

1
2
3
4
5
6
7
8
9
10
11
12
13
14
15
16
17
18
19
20
21
22
23
24
25
26
27
28
29

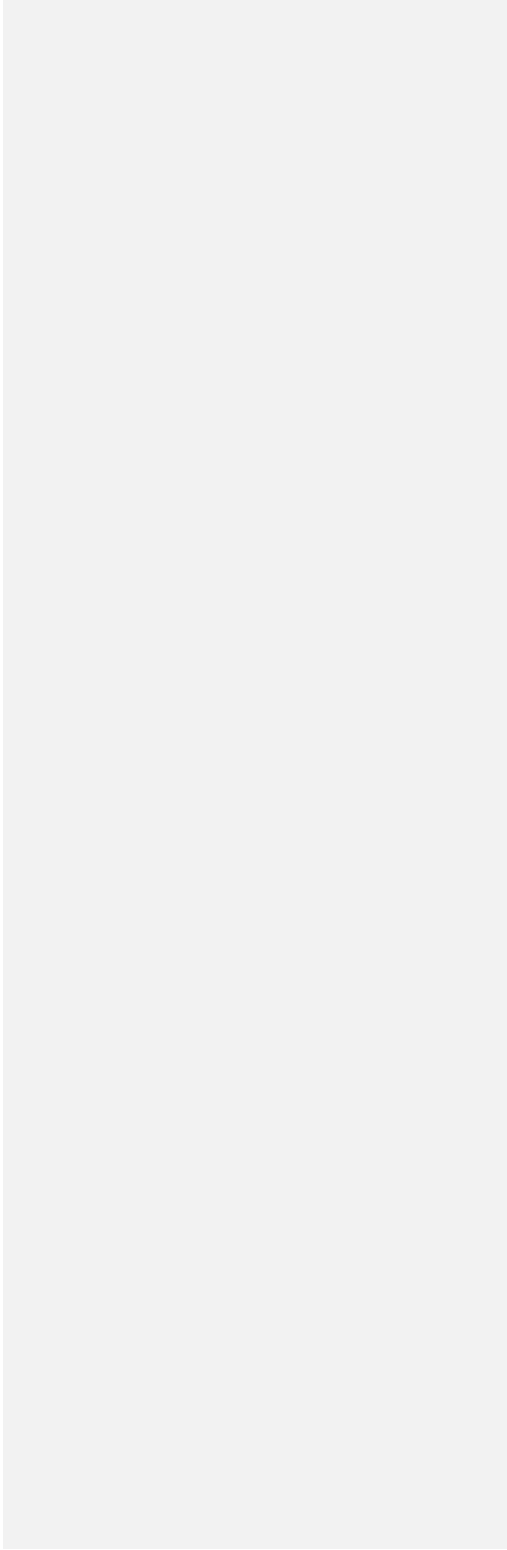
**WAVINESS OF THE SOUTHERN HEMISPHERE WINTERTIME POLAR
AND SUBTROPICAL JETS**

by

Jonathan E. Martin¹ and Taylor Norton²

¹Department of Atmospheric and Oceanic Sciences
²Antarctic Meteorological Research Center
University of Wisconsin-Madison
Madison, WI 53706

Corr. Author: Jonathan E. Martin, jemart1@wisc.edu



Formatted: Header

ABSTRACT

30
31
32
33 The recently developed average latitudinal displacement (ALD) methodology is applied
34 to assess the waviness of the austral winter subtropical and polar jets using three different
35 reanalysis data sets. As in the wintertime Northern Hemisphere, both jets in the Southern
36 Hemisphere have become systematically wavier over the time series and the waviness of each jet
37 evolves quite independently of the other during most cold seasons. Also, like its Northern
38 Hemisphere equivalent, the Southern Hemisphere polar jet exhibits no trend in speed (though it
39 is notably slower) while its poleward shift is statistically significant. In contrast to its Northern
40 Hemisphere counterpart, the austral subtropical jet has undergone both a systematic increase in
41 speed as well as a statistically significant poleward migration. Composite differences between
42 the waviest and least wavy seasons for each species suggest that the Southern Hemisphere's
43 lower stratospheric polar vortex is negatively impacted by unusually wavy tropopause-level jets
44 of either species. These results are considered in the context of trends in the Southern Annular
45 Mode as well as the findings of other related studies.

Deleted: The analysis reveals both similarities and differences between the hemispheres with respect to aspects of the tendencies exhibited by both species of jets over the last 6 decades.

Deleted: creep

Deleted: Finally, composite

46
47 **KEYWORDS:** Southern Hemisphere, winter, polar jet, subtropical jet, waviness
48

1. Introduction

55
56
57 Consideration of changes in the behavior of the tropopause-level jet streams in a warming
58 world has been catalyzed by the construction of long-period reanalysis data sets over the past
59 three decades (Kalnay et al, 1996; Kistler et al., 2001; Kobayashi et al. 2015; Copernicus
60 Climate Change Services [CS3], 2017). Recent analyses employing these data sets (e.g. Archer
61 and Caldiera, 2008; Barnes and Screen, 2015; Gallego et al. 2005; Manney and Hegglin, 2018;
62 Peña-Ortiz et al. 2013; Vavrus et al. 2017), in tandem with a number of studies based upon
63 climate model output (e.g. Barnes and Polvani, 2013; Lorenz and DeWeaver, 2007; Miller et al.
64 2006; Yin, 2005), have produced a consensus view that poleward displacement of both jets
65 accompanies warming. Along with an interest in latitudinal position, nearly all of the
66 aforementioned studies have also addressed either observed and/or forecasted changes in the
67 speed of the jet streams.

68 In a recent paper Martin (2021) offered a feature-based analysis of the *waviness* of the
69 tropopause-level polar and subtropical jets during Northern Hemisphere winter (DJF). The
70 analysis proceeded from the results of Christenson et al. (2017) that identified the isentropic
71 layers that house the two species of jets during NH winter. He found that 1) the polar jet (POLJ)
72 has undergone a statistically significant poleward migration over the time series, not matched by
73 the subtropical jet (STJ), and 2) neither jet species exhibited a trend in its speed. Additionally,
74 the analysis showed that both jets have become systematically wavier over the last 6 decades.

75 By virtue of its land/sea distribution, enhanced lower tropospheric warming at high
76 latitudes of the NH, known as Arctic amplification, has recently emerged as a prominent signal
77 of climate change (e.g., Serreze et al. 2009; Screen and Simmonds, 2013: and references therein).
78 Francis and Vavrus (2012) were among the first to propose that changes in the undulatory nature

79 of the jet stream might be linked to Arctic amplification. This suggestion initiated a decade-long
80 debate on this issue (e.g. Barnes, 2013; Blackport and Screen, 2020; DiCapua and Coumou,
81 2016; Francis, 2017; Francis and Vavrus, 2015; Francis et al. 2018; Martineau et al. 2017, Screen
82 and Simmonds, 2013; Vavrus, 2018). As noted by Martin (2021), at least some of the
83 controversy and attendant lack of consensus surrounding this question (Barnes and Polvani,
84 2015) was nourished by the absence of a robust method of assessing the waviness of the
85 tropopause-level jets. The average latitudinal displacement (ALD) methodology introduced in
86 Martin (2021) (briefly described later) offers one possible remedy to this deficiency.

87 The principle mode of variability in the SH extratropical circulation is the Southern
88 Annular Mode (SAM, Limpasuvan and Hartmann, 1999; Gong and Wang, 1999; Thompson and
89 Wallace, 2000), a nearly zonally symmetric structure with coincident geopotential height
90 anomalies of opposite signs in Antractica and the middle latitudes. In the decades prior to 2000,
91 the SH jets have shifted poleward and the SAM has tended toward positive polarity (e.g. Fogt
92 and Marshall, 2020). These coincident trends have been presumed to be a result of ozone
93 depletion. As the ozone recovers in the SH, simulations suggest a reversal of this trend may be
94 forthcoming (WMO, 2022). Spenberger et al. (2020) have questioned whether the associated jet
95 displacement also explains shifts in the storm tracks across the hemisphere. Instead they suggest
96 that SAM can be interpreted as a measure of the degree of coupling (or decoupling) between
97 Antractica and the southern mid-latitudes.

98 Recently, considerable attention has been devoted to interrogating the zonally
99 asymmetric component of SAM (e.g. Fan 2007; Silvestri and Vera, 2009; Fogt et al. 2012; Rosso
100 et al. 2018; Campetelli et al. 2022). This asymmetric component is characterized by a wave-3
101 pattern (Goyal et al., 2021; Goyal et al., 2022; Campetelli et al. 2022) with maximum amplitude

Formatted: Header

103 at 250 hPa in the Pacific and may be determinative of the overall positive trend in the SAM over
104 the reanalysis era. Such a wave-3, tropopause-level signal is immediately suggestive of the
105 influence of the jets. These observations motivate consideration of direct measurement of the
106 waviness of the SH wintertime jets.

107 Despite a number of recent studies that consider aspects of the interannual variability of
108 the austral winter subtropical jet (e.g. Gillett et al., 2021; Maher et al. 2019), to our knowledge, a
109 study by Gallego et al. (2005) is the only one to consider direct measurement of the waviness of
110 the austral winter jets. They employed an objective method focused on identifying the
111 geostrophic streamline of maximum average velocity at 200 hPa (i.e. the jet core at that level) to
112 separately consider the behaviors of the STJ and POLJ. This method allowed consideration of
113 the jets as continuous features around the hemisphere and thus enabled a number of novel
114 analyses of their behavior and trends. With particular relevance to the present study, they
115 considered a zonal index computed as the difference between the maximum and minimum
116 latitude of the jet core (i.e. the streamline at the core of the jet) on each day. A similar metric,
117 termed DayMaxMin, was employed by Barnes (2013) in her consideration of the behavior of the
118 NH 500 hPa flow. Though insightful, such a metric does not comprehensively account for the
119 waviness created by the full collection of troughs and ridges around the hemisphere that
120 routinely characterizes the jets.

Deleted: aspects

121 In this paper we apply the methodology of Martin (2021) to assess recent trends in the
122 waviness of the SH wintertime polar and subtropical jets. The method of identifying the austral
123 winter polar and subtropical jet locations in isentropic space is described in Section 2 along with
124 a description of the data sets used. Also included there is a short description of the method of
125 assessing waviness introduced in Martin (2021). In Section 3, elements of the long-term trend

127 and interannual variability of the waviness of the austral winter polar and subtropical jets are
128 presented along with differences between composites of the waviest and least wavy seasons for
129 each species. A summary and conclusions are offered in Section 4.

130

131 2. Data and Methodology

132

133 In the foregoing analysis, the zonal (u) and meridional (v) winds as well as temperature (T),
134 at 6 h intervals from three different reanalysis data sets are employed. 72 austral winters (JJA)
135 (1948-2019) of the National Centers for Environmental Prediction/National Center for
136 Atmospheric Research (NCEP/NCAR) reanalysis, at 17 isobaric levels to 10 hPa on a 2.5°
137 latitude-longitude grid (Kalnay et al., 1996; Kistlet et al., 2001) are used. We employ 62 winters
138 (1958-2019) of the Japanese 55-year (JRA-55) reanalysis with data on 60 vertical levels up to 0.1
139 hPa on a horizontal grid mesh of ~55 km (Kobayashi et al., 2015). Finally, the ERA5 reanalysis
140 data set on 137 vertical levels from the surface to 80 km with a grid spacing of 31 km covering
141 the period from 1979 to 2019 (Copernicus Climate Change Service [CS3], 2017) are used as
142 well. The waviness of the jets is assessed in the context of understanding their relationships to
143 the horizontal gradient of potential vorticity (PV) in prescribed isentropic layers. A similar
144 approach was taken with respect to the STJ in recent work by Maher et al. (2019). The first step
145 in the present analysis involves identification of the isentropic layers that house the austral winter
146 jets. This was accomplished empirically by identifying the isentropic level at which the
147 maximum wind speed was observed in each grid column (between 10 and 80°S) at each analysis
148 time in JJA over the 62-year time series of the JRA-55 data set. The use of isentropic space here
149 differs from the insightful approach taken by Manney et al. (2017) and Manney and Hegglin

Deleted: , therefore,

151 [\(2018\) which employed separate latitude and elevation criteria to differentiate between the STJ](#)
152 [and the POLJ.](#) Of the three data sets employed in the present work, the JRA-55 was chosen for
153 this preliminary analysis step because both its length of time series as well as its horizontal and
154 vertical resolutions are between those characterizing the other two data sets employed here.
155 Following Koch et al. (2006) we only considered columns in which the integral average wind
156 speed exceeded 30 ms^{-1} in the 100-400 hPa layer. The resulting distribution is clearly tri-modal
157 with frequency maxima, and therefore separate jet features, approximately located in the 305-
158 320, 340-355, and 395-410K isentropic layers (Fig. 1a). The latter isentropic layer appears in the
159 lower stratosphere and is associated with the austral polar night jet (PNJ), which, being located
160 *above* the tropopause, is not a focus of the present analysis. Further separation of the STJ and
161 POLJ is achieved through reference to Fig. 2 of Gallego et al. (2005) which strongly implies that
162 the STJ sharply peaks near 30°S while the POLJ more broadly peaks around 50°S . Accordingly,
163 we further constrained the analysis to latitude bins $0\text{-}40^{\circ}\text{S}$ for the STJ and $40\text{ to }65^{\circ}\text{S}$ for the
164 POLJ. With this additional refinement, the analysis identifies the STJ in the 340-355K isentropic
165 layer and the POLJ in the 310-325K isentropic layer (Fig. 1b). Similar analyses of the other two
166 data sets (not shown) revealed the robustness of this result. It is important to note that 53.8% of
167 all qualifying columns (to 380K) in the $0\text{-}40^{\circ}\text{S}$ bin (STJ) were in the 340-355K layer while
168 46.8% of all qualifying columns in the $40\text{-}65^{\circ}\text{S}$ bin (POLJ) were in the 310-325K layer,
169 [supporting the isentropic assignments for the two species mentioned previously.](#) It is
170 immediately apparent, consistent with prior analyses (e.g. Bals-Elsholz et al. 2001, Nakamura
171 and Shimpo 2004, Gallego et al. 2005), that the STJ is the dominant jet feature in the southern
172 winter.

174 The analysis method to be used here involves assessment of the circulation which
175 requires calculation of contour length. As a result, fair comparison among the different data sets
176 requires adoption of a uniform grid spacing. Consequently, all three data sets were bilinearly
177 interpolated onto isentropic surfaces at 5K intervals (from 280 to 380K) and 2.5° latitude-
178 longitude grid spacing using programs within the General Meteorological Analysis Package
179 (GEMPAK) (desJardins et al., 1991). The average PV and average zonal and meridional wind
180 speeds in both the polar jet (310:325K) and subtropical jet (340:355K) layers were then
181 calculated from the four times daily data for each day in each of the three time series.
182 As reviewed in Martin (2021), consideration of the quasi-geostrophic potential vorticity
183 (QGPV), following Cunningham and Keyser (2004), demonstrates that local maxima in the
184 cross-flow gradient of QGPV are collocated with maxima in the geostrophic wind speed. In the
185 Southern Hemisphere, the jets lie on the high PV edge of this PV gradient. By searching through
186 daily average isertels from -0.5 to -5.0 at 0.1 PVU intervals ($1 \text{ PVU} = 10^{-6} \text{ m}^2 \text{ K kg}^{-1} \text{ s}^{-1}$), the
187 analysis identifies a “core isertel” along which the circulation per unit length (i.e. average speed)
188 is maximized in the separate POLJ (310:325K) and STJ (340:355K) isentropic layers for every
189 day in each of the time series. This core isertel is, by design, an analytical proxy for the jet core.
190 A glimpse into the fidelity of this method in identifying the meandering cores of the POLJ and
191 STJ jets is illustrated in Fig. 2. In each case the objectively identified core isertel, in black, lies
192 very near, or at, the center of the analyzed isotach maxima around the hemisphere with
193 physically defensible exceptions. For instance, the red dashed lines in Fig. 2b indicate portions
194 of the bold black line in Fig. 2d (i.e. the overlying STJ core) suggesting that those portions of the
195 isotach maxima in Fig. 2b that are somewhat removed from the POLJ core isertel are the lower
196 portions of the overlying STJ core. Similarly, an extensive isotach maxima region in Fig. 2d has

197 a blue dashed line, a portion of the bold black line in Fig. 2b, slicing through it. This region,
198 well poleward of the STJ core isertel, is clearly the upper portion of the underlying POLJ core.

199 Figure 3a shows the average latitude for the core isertels of each jet species from each of the
200 three reanalyses data sets used in the study. The analyses return essentially identical results for
201 the core isertel of the STJ and very nearly identical results for the POLJ. Superimposing the
202 NCEP-NCAR reanalysis' JJA average 200 hPa isotachs on top of the STJ core isertels (Fig. 3b)
203 illustrates the fact that the average core isertel accurately represents the axis of the average STJ.
204 The relationship is also strong between the POLJ core isertels and the 700 hPa average isotachs
205 (Fig. 3c).

206 The waviness of each jet is assessed by calculating a hemispheric average of the meridional
207 displacements of the core isertel from its equivalent latitude – the northern extent of a polar cap
208 whose area is equal to the area enclosed by the core isertel. This metric is referred to as the
209 average latitudinal displacement (ALD). The method does not require that the core isertel be the
210 same in both jet layers on a given day, nor that it be the same from day-to-day in a given jet
211 layer. Consequently, it is important to examine its distribution in each jet layer over the entire
212 time series. Figure 4 portrays the frequency of occurrence of the core isertels in both the STJ
213 and POLJ layers for each of the three time series. The STJ core isertels peak between -1.95 and -
214 2.1 PVU across the three data sets. Considering all three data sets, 81.5% of all JJA days exhibit
215 a core isertel between -1 and -3 PVU in the STJ layer. The POLJ distribution is shifted toward
216 higher PV values. Overall, 74.8% of JJA days had a core isertel between -1 and -3 PVU in the
217 POLJ layer. The frequency of occurrence in the several isertelic bins for each species of SH jet
218 match quite well with what Martin (2021) found for the NH wintertime jets, even when
219 accommodating for the different isentropic layer for the austral POLJ.

221

222 3. Analysis

223

224 The JJA seasonal average latitudinal displacement (ALD) of each jet is calculated as a

225 92-day average of the daily ALD in each cold season. The results are shown in Fig. 5. It is

226 instantly clear that, as in the NH, the POLJ is wavier than the STJ and that both jets have become

227 systematically wavier over the 62-year JRA-55 time series with $p < 0.004$ for both time series (a

228 one-sided Student's t -test was employed). Interestingly, the austral winter STJ is less wavy than

229 its NH counterpart but the waviness of both has increased identically at 0.005 deg/yr ~~(0.0125~~

230 ~~deg/yr for NCEP since 1958 and -0.001 deg/yr for ERA-5)~~. The winter POLJ in the SH is, on

231 the other hand, wavier than in the NH and is trending faster (0.017 versus 0.009 deg/yr: ~~0.023~~

232 ~~deg/yr for NCEP since 1958 and 0.009 deg/yr for ERA-5)~~ than its NH complement. Daily time

233 series of the ALD of each jet can also be examined to determine the extent to which the waviness

234 of the two jets covaries. Figure 6 illustrates the POLJ and STJ daily ALDs for 1999 from each of

235 the three data sets. The low correlation between the waviness of the two species in this example

236 year represents the rule rather than the exception. All told, more than 93% of the STJ and POLJ

237 ALD seasonal time series constructed for this study are correlated with magnitudes less than 0.3.

238 This result strongly suggests that the waviness of the two species evolves independently.

239 By definition, the average wind speed along the chosen core isertel on any given day

240 represents the average jet speed for that species on that day. Time series of seasonal average jet

241 core wind speeds for the wintertime STJ and POLJ in both hemispheres are shown in Fig. 7. As

242 in the NH winter (Martin, 2021), the austral POLJ shows almost no trend in jet core speed and

243 the slight change is not statistically significant. Notably, however, the SH POLJ is $\sim 6 \text{ m s}^{-1}$

Formatted: Header

Deleted: 4

Deleted: .

Deleted: 5

Formatted: Indent: First line: 0.5"

Deleted: 6

248 slower on average than its NH equivalent. Aside from the fact that the NCEP reanalysis is quite
249 different from the JRA-55 until about 1970, the austral winter STJ exhibits a robust, and
250 statistically significant (p -value < 0.001), increase in speed over the JRA-55 time series – in clear
251 contrast to its NH counterpart. It is also apparent that the SH STJ is slightly weaker but less
252 interannually variable than the NH STJ.

253 Another characteristic of interest that emerges directly from the ALD analysis method is
254 the daily value of the jet core's equivalent latitude which closely approximates its zonally
255 averaged position. Consequently, it is straightforward to construct a time series of the seasonal
256 average equivalent latitudes of the two species of jets, shown in Fig. 8. Again, as in the NH, the
257 poleward shift of the SH POLJ is occurring three times faster than that exhibited by the STJ. In
258 contrast to the situation in the NH, however, the slight poleward displacement of the SH STJ *is*,
259 like that of the POLJ, statistically significant (p -values for the POLJ and STJ are < 0.001 and
260 0.002 , respectively). It is interesting to note that while the SH STJ is located at a roughly similar
261 latitude as the NH STJ throughout the time series, the SH POLJ is $\sim 4^\circ$ further poleward during
262 winter than the NH POLJ. Overall, a much more systematic and dramatic poleward migration of
263 the two jets has occurred over the last 6 decades in SH winter as compared to NH winter.

264 Next we consider aspects of the analysis in the context of the SAM. Figure 9 shows a
265 histogram of the JJA average SAM index (calculated after Gong and Wang (1999))
266 superimposed upon the average JJA ALD from the JRA-55 reanalysis. The tendency toward
267 positive SAM over the time series appears to be reflected in the increase in ALD. However, the
268 correlation between the two time series is 0.053 suggesting almost no relationship exists between
269 the two.

Formatted: Header

Deleted: ¶

Deleted: represents

Deleted: 7

Deleted: creep

Deleted: →

Formatted: Header

275 In order to investigate the relationship of ALD to extremes in the polarity of the SAM
276 index, the three winter months with the most positive and most negative SAM extremes since
277 1979 were considered. The core isertels of the POLJ (from the JRA-55 reanalysis) for each of
278 these three months is portrayed in Fig. 10. Positive extremes of SAM (Figs. 10a, c, and e) show
279 a clear poleward encroachment of the SH polar jet while negative extremes (Figs. 10b, d, and f)
280 suggest the opposite. There appears to be no systematic connection, however, between extremes
281 in SAM and the waviness of the POLJ as quantified by ALD.

282 Thus far the analysis has presented elements of the seasonal average behavior of the
283 austral winter jet species. The methodology, of course, allows for evaluation of daily time series
284 of ALD as well and, in fact, such an analysis underlies the presentation in Fig. 6. Using such
285 daily time series, identification of the waviest and least wavy seasons for each jet species since
286 1979 is accomplished by summing the daily departures from calendar-day average ALD over the
287 92 days of each cold season. The list of such seasonally integrated departures from average
288 waviness for each species of jet for each reanalysis data set is shown in Table 1. From this list,
289 the 5 waviest and 5 least wavy seasons for each jet species were selected to construct composites
290 of geopotential height at several isobaric levels employing the JRA-55 data. In the foregoing
291 analysis, height differences are obtained by subtracting values associated with the composite
292 least wavy seasons from those associated with the composite waviest seasons.

293 Figure 11a shows the 500 hPa geopotential height differences between the waviest and
294 least wavy POLJ seasons. Wavy POLJ years are characterized by positive height anomalies over
295 the continent and adjacent to its east and west coasts with belts of negative anomalies in a
296 crescent stretching from southwest of Chile and then extending from the east coast of South
297 America to southern Africa toward Australia, suggestive of a negative SAM. The strongest

Formatted: Indent: First line: 0.5"

Deleted: 5

Deleted: 8a

Deleted: .

301 negative height anomalies in such seasons occur west of South Africa implying a slight
302 weakening of the zonal winds just south of the Cape of Good Hope. Meanwhile wavy STJ years
303 exhibit negative composite height differences in roughly the same locations as the positive
304 composite differences just described for wavy POLJ years (Fig. 11b), suggestive of a positive
305 SAM. These composite difference patterns strengthen slightly at 250 hPa (Fig. 12) suggesting an
306 equivalent barotropic structure to the tropospheric portion of the difference fields.

307 The difference fields at 50 hPa imply that the waviness of both jets exerts an
308 influence on the strength of the austral polar vortex in the lower stratosphere. The anomalous
309 height field associated with wavy POLJ years (Fig. 13a) suggests a broad, though modest,
310 anticyclonic circulation anomaly just off the pole in the Western Hemisphere. Such a
311 perturbation flow would appear to interfere with the establishment and/or persistence of strong
312 vortex flow in the same location. Wavy STJ seasons also impose a dipole of positive heights the
313 axis of which stretches from Cape Horn to East Antarctica (Fig. 13b). Such a configuration
314 implies that the polar vortex is both weaker and displaced off the pole in winters with wavy
315 STJs. Thus, the analysis suggests that in winters characterized by unusually wavy jets of either
316 species, the SH polar vortex is likely weaker than normal. Further investigation of this intriguing
317 implication is the subject of ongoing work.

318 319 4. Summary

320
321 The analysis presented here extends the application of a method developed by Martin
322 (2021) to assess the waviness of the tropopause-level jets to analysis of the austral winter polar
323 and subtropical jets. The analysis demonstrates that both jets have become systematically wavier

Formatted: Header

Deleted: 8b).

Deleted: 9

Deleted: 10a

Deleted: 10b

328 over the past 60+ years. In addition, as in the NH, the waviness of the two species of austral
329 winter jets is largely uncorrelated suggesting little systematic influence of one on the other
330 throughout the season. Along with these similarities, there appear to be some fundamental
331 asymmetries in the behavior of the wintertime tropopause-level jets between the hemispheres.
332 The austral POLJ, like its NH counterpart, has exhibited no trend in its average speed over the
333 time series, though it is notably slower than its NH wintertime equivalent. The STJ, on the other
334 hand, has roughly the same speed as that in the NH winter but, unlike its NH counterpart, has
335 undergone a systematic, statistically significant increase in its core speed since ~1960.
336 Additionally, as opposed to the situation in the NH where only the POLJ migration toward to
337 pole is statistically significant, *both* SH jets exhibit a significant poleward creep with the POLJ
338 encroachment occurring at ~3x the rate of that characterizing the STJ.

339 The observed poleward migration of the STJ reported here is consistent with the analysis
340 of CMIP5 simulations of historical and projected changes to the SH wintertime STJ by Chenoli
341 et al. (2017). Though the present work employs a similarly dynamical definition of the STJ as
342 that used in the study by Maher et al. (2019), they found no evidence of a poleward shift of the
343 SH wintertime STJ. We suggest that the emphasis on empirically identifying a core isertel,
344 rather than the maximum gradient of θ on a predetermined isertelic surface (i.e. 2 PVU as the
345 dynamic tropopause) may account for this difference.

346 Finally, circulation differences between the waviest and least wavy POLJ and STJ
347 seasons are manifest in both the troposphere and lower stratosphere. In the troposphere the
348 signals are not as coherent in the SH as they were revealed to be in the NH (Martin 2021).
349 Interestingly, the analysis implies that when either the POLJ or STJ is wavier than normal in a

Formatted: Header

350 given winter, the lower stratospheric polar vortex is negatively impacted. Again, this is different
351 from the behavior of the NH polar vortex in the face of extremes in waviness.

352 The results presented here, combined with those in Martin (2021), demonstrate that in
353 both hemispheres a wavier than normal STJ during winter serves to weaken the lower
354 stratospheric polar vortex. Though, as suggested by the analysis supporting Fig. 6, the STJ and
355 POLJ do not appear to influence one another systematically, there are still instances in which the
356 waviness of the two jets can be phased so as to promote intense interactions. Daily perusal of
357 hemispheric synoptic maps suggests that such instances of jet interaction often lead to intense
358 lower tropospheric cyclogenesis events. Current research is examining whether such jet
359 interaction-induced cyclogenesis events from specific seasons systematically correspond to
360 episodes of polar vortex weakening.

Deleted: 5

Deleted: The polar vortex can be weakened by the absorption of vertically propagating planetary waves originating from such developments (Matsuno, 1971). Thus, intense cyclogenesis, encouraged by wavy and well phased POLJ and STJs, may underlie the association, revealed here, between tropopause-level jet waviness and polar vortex strength during austral winter.

361
362 COMPETING INTERESTS: The contact author has declared that none of the authors has any
363 competing interests.

364
365 AUTHOR CONTRIBUTIONS: J. Martin completed the ALD analysis and did all the writing,
366 figure drafting and preparation of the manuscript for submission. T. Norton performed the
367 analysis that determined the POLJ and STJ isentropic housings during SH winter.

368
369 ACKNOWLEDGEMENTS: This work was supported by the National Science Foundation under
370 grants ATM-1640055 and NSF-2055667. JRA-55 data available from the Research Data
371 Archive at the National Center for Atmospheric Research. The authors would like to thank Prof.
372 Andrea A. Lopez-Lang for helpful comments and suggestions.

REFERENCES

381

382

383 Archer, C. L., and K. Caldeira, 2008: Historical trends in the jet stream. *Geo. Res. Let.*, **35**(8).

384

385 Bals-Elsholz, T. M., E. H. Atallah, L. F. Bosart, T. A. Wasula, M. J. Cempa, and A. R. Lupo,
386 2001: The wintertime Southern Hemisphere split jet: Structure, variability, and evolution.
387 *J. Climate*, 14, 4191-4215.

388

389 Barnes, E. A., 2013: Revisiting the evidence linking Arctic amplification to extreme weather in
390 midlatitudes. *Geophys. Res. Let.*, **40**, 4734-4739.

391

392 _____, and L. Polvani, 2013: Response of the midlatitude jets, and of their variability, to
393 increased greenhouse gases in the CMIP5 models. *J. Climate*, 26, 7117-7135.

394

395 _____, and J. A. Screen, 2015: The impact of Arctic warming on the midlatitude jet-stream: Can
396 it? Has it? Will it? *WIREs Clim Change*, **6**, 277–286. doi: 10.1002/wcc.337.

397

398 Blackport, R., and J. A. Screen, 2020: Insignificant effect of Arctic amplification on the
399 amplitude of midlatitude atmospheric waves. *Science advances*, 6(8), p.eaay2880.

400

401 [Campitelli, E., L. B. Diaz, and C. Vera, 2021: Assessment of zonally symmetric and asymmetric](#)
402 [components of the Southern Annular Mode using a novel approach. *Clim. Dyn.*, **58**, 161-](#)
403 [178.](#)

404 [Chenoli, S. N., M. Y. Ahmad Mazuki, J. Turner, & A. A. Samah, 2017: Historical and projected](#)
405 [changes in the Southern Hemisphere sub-tropical Jet during winter from the CMIP5](#)
406 [models. *Clim. Dyn.*, **48**, 661-681.](#)

408 Christenson, C. E., J. E. Martin, and Z. J. Handlos, 2017: A synoptic-climatology of Northern
409 Hemisphere, cold season polar and subtropical jet superposition events. *J. Climate*, **30**,
410 7231-7246.

412 Copernicus Climate Change Service (C3S) (2017): ERA5: Fifth generation of ECMWF
413 atmospheric reanalyses of the global climate. Copernicus Climate Change Service
414 Climate Data Store (CDS), *March 2020*, <https://cds.climate.copernicus.eu/cdsapp#!/home>

416 Cunningham, P., and D. Keyser, 2004: Dynamics of jet streaks in a stratified quasi-geostrophic
417 atmosphere: Steady-state representations. *Quart. J. Roy. Meteor. Soc.*, **130**, 1579-1609.

419 desJardins, M. L., K. F. Brill, and S. S. Schotz, 1991: GEMPAK 5 Part I—GEMPAK 5
420 programmer's guide. National Aeronautics and Space Administration. [Available from
421 Scientific and Technical Information Division, Goddard Space Flight Center,
422 Greenbelt, MD 20771.].

423 DiCapua G., and D. Coumou, 2016: Changes in the meandering of the Northern Hemisphere
424 circulation. *Environ. Res. Lett.*, **11**, 094028, doi:10.1088/1748-9326/11/9/094028.

427 [Fan, K.: Zonal asymmetry of the Antarctic Oscillation. *Geophys. Res. Lett.*,](#)

428 <https://doi.org/10.1029/2006GL028045>.

429

430 [Fogt, R. L., J. M. Jones, and J. Renwick, 2012: Seasonal zonal asymmetries in the Southern](#)

431 [Annular Mode and their impact on regional temperature anomalies. *J. Climate*, **25**, 6253-](#)

432 [6270.](#)

433

434 [Fogt, R. L. and G. J. Marshall, 2020: The Southern Annular Mode: Variability, trends, and](#)

435 [climate impacts across the Southern Hemisphere. *WIREs Climate Change*, **11**\(4\):e652.](#)

436 <https://doi.org/10.1002/wcc.652>.

437

438 Francis, J. A., 2017: Why are Arctic linkages to extreme weather still up in the air?. *Bull. Amer.*

439 *Meteor. Soc.*, **98**, 2551-2557.

440

441 _____, and S. J. Vavrus, 2012: Evidence linking Arctic amplification to extreme weather in mid-

442 latitudes. *Geophys. Res. Lett.*, **39**, L06801, doi:10.1029/2012GL051000.

443

444 _____, and _____, 2015: Evidence for a wavier jet stream in response to rapid Arctic warming.

445 *Environ. Res. Lett.* **10**, 014005, doi:10.1088/1748-9326/10/1/014005.

446

447 _____, N. Skific, and S. J. Vavrus, 2018: North American weather regimes are becoming more

448 persistent: Is Arctic amplification a factor? *Geophys Res. Lett.*,

449 <https://doi.org/10.1029/2018GL080252>.

450

451 Gallego, D., P. Ribera, R. Garcia-Herrera, E. Hernandez, and L. Gimeno, 2005: A new look for

452 the Southern Hemisphere jet stream. *Climate Dyn.*, **24**, 607-621.

453

454 [Gillett, Z. E., H. H. Hendon, J. M. Arblaster, and E.-P. Lim, 2021: Tropical and extratropical](#)
455 [influences on the variability of the Southern Hemisphere wintertime subtropical jet. *J.*](#)
456 [Climate, **34**, 4009-4022.](#)

457

458 [Gong, D., and S. Wang, 1999: Definition of Antarctic oscillation index. *Geophys. Res. Lett.*, **26**,](#)
459 [459-462.](#)

460

461 [Goyal, R., M. Jucker, A. Sen Gupta, H. H. Hendon, and M. H. England, 2021: Zonal wave 3](#)
462 [pattern in the Southern Hemisphere generated by tropical convection. *Nat. Geosci.*, **14**,](#)
463 [732-738.](#)

464

465 [_____, _____, _____, and M. H. England, 2022: A new zonal wave-3 index for the Southern](#)
466 [Hemisphere. *J. Climate*, **35**, 5137-5149.](#)

467

468 Kalnay, E. and co-authors, 1996: The NCEP/NCAR 40-year reanalysis project. *Bull. Amer.*
469 *Meteor. Soc.*, **77**, 437-470.

470

471 Kistler, R. and co-authors, 2001: The NCEP-NCAR 50-Year reanalysis: Monthly means CD-
472 ROM and documentation. *Bull. Amer. Meteor. Soc.*, **82**, 247-267.

473

474 Kobayashi, S., Y. Ota, Y. Harada, A. Ebata, M. Moriya, H. Onoda, K. Onogi, H. Kamahori, C.

- 475 Kobayashi, H. Endo, K. Miyaoka, and K. Takahashi, 2015: The JRA-55 reanalysis:
476 General specifications and basic characteristics. *J. Meteor. Soc. Japan*, **93**, 5-48.
477
- 478 Koch, P., H. Wernli, and H. C. Davies, 2006: An event-based jet-stream climatology and
479 typology. *Int. J. Climatology*, **26**, 283-301.
480
- 481 [Limpasuvan, V., and D. L. Hartmann, 1999: Eddies and the annular modes of climate](#)
482 [variability. *Geophys. Res. Lett.*, **26**, 3133–3136.](#)
483
- 484 Lorenz, D. J., and E. T. DeWeaver, 2007: Tropopause height and zonal wind response to global
485 warming in the IPCC scenario integrations. *J. Geophys. Res: Atmos.*, **112**(D10).
486
- 487 [Maher, P., M. E. Kelleher, P. G. Sansom, and J. Methven, 2020: Is the subtropical jet shifting](#)
488 [poleward?. *Clim. Dyn.*, **54**, 1741-1759.](#)
489
- 490 [Manney, G.L., M. I. Hegglin, Z. D. Lawrence, K. Wargan, L. F. Millán, M. J. Schwartz, M. L.](#)
491 [Santee, A. Lambert, S. Pawson, B. W. Knosp, and R. A. Fuller, 2017: Reanalysis](#)
492 [comparisons of upper tropospheric–lower stratospheric jets and multiple](#)
493 [tropopauses. *Atmos. Chem. and Phys.*, **17**, 11541-11566.](#)
494
- 495 Manney, G. L., and M. I. Hegglin, 2018: Seasonal and regional variations of long-term changes
496 in upper-tropospheric jets from reanalyses. *J. Climate*, **31**, 423-448.
497

498 Martin, J. E., 2021: Recent trends in the waviness of the Northern Hemisphere wintertime polar
499 and subtropical jets. *JGR Atmos.*, <https://doi.org/10.1029/2020JD033668>.

500

501 Martineaux, P., G. Chen, and D. A. Burrows, 2017: Wave events: Climatology, trends, and
502 relationship to Northern Hemisphere blocking and weather extremes. *J. Climate*, **30**,
503 5675-5697.

504

505 Matsuno, T., 1971: A dynamical model of the stratospheric sudden warming. *J. Atmos. Sci.*, **28**,
506 1479-1494.

507

508 Miller, R. L., G. A. Schmidt, and D. T. Shindell, 2006: Forced annular variations in the 20th
509 century Intergovernmental Panel on Climate Change Fourth Assessment Report models.
510 *J. Geophys. Res.*, **111**, D18101, doi:10.1029/2005JD006323.

511

512 Nakamura, H., and A. Shimpo, 2004: Seasonal variations in the Southern Hemisphere storm
513 tracks and jet streams as revealed in a reanalysis data set. *J. Climate*, **17**, 1828-1844.

514

515 Peña-Ortiz, C., D. Gallego, P. Ribera, P. Ordonez, and M. D. C. Alvarez-Castro, 2013: Observed
516 trends in the global jet stream characteristics during the second half of the 20th century,
517 *J. Geophys. Res. Atmos.*, **118**, 2702–2713, doi:10.1002/jgrd.50305.

518

519 [Rosso, F. V., N. T. Boiaski, S. E. T. Ferraz, and T. C. Robles, 2018: Influence of the Antarctic](#)
520 [oscillation on the South Atlantic convergence Zone. *Atmosphere*, 9\(11\), 431.](#)

521

522 Screen, J. A., and I Simmonds, 2013: Exploring links between Arctic amplification and mid-
523 latitude weather. *Geophys. Res. Lett.*, <https://doi.10.1002/grl.50174>.

524

525 Serreze, M.C., A. P. Barrett, J. C. Stroeve, D.N Kindig. and M.M. Holland, 2009: The
526 emergence of surface-based Arctic amplification. *Cryosphere*, **3**, 11-19.

527

528 [Silvestri, G., and C. Vera, 2009: Nonstationary impacts of the Southern Annular Mode on
529 Southern Hemisphere climate. *J. Climate*, **22**, 6142–6148.](#)

530

531 [Spensberger, C., M. J. Reeder, T. Spengler, and M. Patterson, 2020: The connection between the
532 Southern Annular Mode and a feature-based perspective on Southern Hemisphere
533 midlatitude winter variability. *J. Climate*, **33**, 115.129.](#)

534

535 [Thompson, D., and J. Wallace, 2000: Annular modes in the extratropical circulation. Part I:
536 Month-to-month variability. *J. Climate.*, **13**, 1000-1016.](#)

537

538 Vavrus, S. J., 2018: The influence of Arctic amplification on mid-latitude weather and climate.
539 *Curr. Clim. Change. Rep.*, **4**, 238-249.

540

541 _____, F. Wang, J. E. Martin, J. A. Francis, Y. Peings, and J. Cattiaux, 2017: Changes in North
542 American circulation and extreme weather: Influence of arctic amplification and
543 Northern Hemisphere snow cover. *J. Climate* , **30**, 4317-4333.

|

544

545 WMO. 2022. Executive summary. Scientific assessment of ozone depletion: 2022. GAW report

546 no. 278. Geneva, Switzerland: WMO

547 Yin, J. H., 2005: A consistent poleward shift of the storm tracks in simulations of 21st century

548 climate. *Geophys. Res. Let.*, **32**, L18701,doi:10.1029/2005GL023684.

549

Formatted: Header

Formatted: Line spacing: Double

	<i>POLJ</i>			<i>STJ</i>		
	<i>NCEP</i>	<i>JRA-55</i>	<i>ERA5</i>	<i>NCEP</i>	<i>JRA-55</i>	<i>ERA5</i>
1979	-45.416403	-19.684881	-64.232707	-3.7754167	11.1345645	0.70639878
1980	-59.380403	-58.393881	-63.657707	-3.2564167	4.47656452	-0.8576012
1981	18.8845972	36.4021194	21.8872927	-4.4154167	5.17956452	-2.2326012
1982	-24.813403	3.63785707	-15.198707	41.2785833	16.1355645	10.5773988
1983	-16.281403	35.8650731	-15.658707	-18.131417	-10.037435	-21.992601
1984	-14.954403	4.06711936	-6.9887073	15.8335833	19.8715645	11.5133988
1985	4.02659722	10.3371194	-20.535707	54.3615833	38.7185645	21.4393988
1986	24.2525972	43.6271194	20.5902927	-6.9904167	0.00256452	-10.285601
1987	62.9565972	77.0631194	16.8692927	-8.9194167	0.57256452	-9.2566012
1988	-2.5614028	-7.4278806	-35.518707	-1.9554167	2.34556452	-5.2936012
1989	-33.646403	9.93808658	-16.752707	35.2235833	29.6575645	19.4843988
1990	21.8045972	40.1761194	5.93129268	28.6225833	8.32356452	-0.0366012
1991	98.1615972	104.846187	79.9922927	15.9005833	13.6185645	10.0163988
1992	-31.301403	-26.480881	-43.682707	23.9145833	30.1255645	22.5733988
1993	45.9685972	64.4221194	23.6692927	-5.4784167	7.54756452	-0.9296012
1994	-29.454403	-32.656881	-69.886707	51.5895833	30.9815645	21.4813988
1995	-22.226403	-20.908881	-47.179707	-5.1054167	-12.989435	-16.721601
1996	80.0555972	96.1361194	86.8222927	-2.3444167	-10.092435	-11.395601
1997	68.8895972	57.6655297	78.5282927	2.23058333	-8.3644355	-11.693601
1998	-27.166403	-32.68934	-70.988707	18.5915833	-2.3754355	-7.9706012
1999	36.1115972	-22.593881	-44.562707	3.60158333	-23.970435	-32.015601
2000	57.1715972	17.3883325	16.0832927	49.9395833	18.8905645	12.2183988
2001	51.6315972	26.2991194	8.28429268	46.9905833	7.20656452	1.48939878
2002	30.0675972	35.9181194	21.4212927	65.2545833	47.0115645	40.0813988
2003	70.6935972	52.1291194	24.5692927	12.5915833	-3.7804355	-11.507601
2004	27.8395972	-18.835881	-31.660707	39.5535833	19.0855645	13.4163988
2005	48.0095972	26.0351194	-2.9987073	-10.510417	-21.297435	-26.212601
2006	76.9665972	27.7838267	24.9342927	29.3135833	-2.1904355	-10.139601
2007	60.9595972	55.4256292	46.9952927	38.6865833	17.2975645	14.1103988
2008	67.6425972	67.2851194	66.7882927	-4.0874167	-21.790435	-25.102601
2009	69.9215972	17.7955696	23.8622927	22.6285833	-4.6854355	-8.0676012
2010	41.5965972	13.4191194	3.93329268	31.9945833	16.0065645	11.1233988
2011	118.932597	111.764119	79.1722927	11.7745833	-5.6934355	-8.7496012
2012	38.3955972	9.84011936	-2.5287073	54.8005833	14.8235645	-1.2216012
2013	32.3355972	-0.7048806	-14.266707	67.4165833	25.3645645	13.6133988
2014	52.2325972	45.4011194	-60.736707	40.1415833	20.9895645	6.32532378
2015	65.0135972	38.0481194	18.8882927	14.6575833	1.69656452	-1.7356012
2016	51.9375972	19.3210046	15.3602927	22.3815833	2.71556452	-0.3676012
2017	15.4975972	-14.224881	-38.558707	30.2145833	2.97356452	-2.2008762
2018	70.8755972	21.0891194	3.86429268	3.15258333	-7.7994355	-11.277601
2019	68.5365972	5.97811936	-22.852707	58.1465833	21.7315645	7.09439878

TABLE 1 Integrated seasonal departures from average ALD (degrees) for polar and subtropical jets from the three reanalysis data sets employed in this work. Gray (light blue) shading represents one of the top 5 waviest (least wavy) seasons.

FIGURE CAPTIONS

551

552

553 Fig. 1 (a) Distribution of grid-column maximum wind speeds found in 5K isentropic layers from
554 10 - 80°S for every 6h analysis time in JJA from 1958-2019 from the JRA-55 reanalysis. (b) As
555 for Fig. 1a except limited to (i) grid-columns in which the integral average wind speed from 400
556 to 100 hPa exceeded 30 m s^{-1} and (ii) to latitudes 0 - 40°S for the STJ and (iii) latitudes 40 to
557 65°S for the POLJ.

558

559 Fig. 2 (a) Isotachs of the daily averaged wind speed (contoured every 10 m s^{-1} and shaded above
560 30 m s^{-1}) and the core isertel (bold black line) in the 310:325K isentropic layer on 13 July 1995
561 from the JRA-55 reanalysis data. The core isertel value is -1.3 PVU. (b) As in (a) but for 24
562 August 2001. Core isertel value is -2.0 PVU. Dashed red line indicates portion of the core
563 isertel from the overlying STJ layer (depicted in Fig. 2d). (c) As in (a) but for wind speeds and
564 core isertel in the 340:355K isentropic layer on 13 July 1995. Core isertel value is -3.6 PVU. (d)
565 As in (c) but for 24 August 2001. Core isertel value is -1.4 PVU. Dashed blue line indicates a
566 portion of the core isertel from the underlying POLJ layer (depicted in Fig. 2b). See text for
567 further explanation.

568

569 Fig. 3 (a) Solid (dashed) lines are the positions of the average core isertels of the STJ (POLJ)
570 from each of the three reanalyses employed in this study. The different reanalyses are color
571 coded. (b) Thick solid lines are the positions of the average core isertels for the STJ from each
572 of the reanalyses superimposed with JJA average 200 hPa isotachs from the NCEP-NCAR

574 reanalysis. (c) Thick dashed lines are the positions of the average core isertels for the POLJ
575 superimposed with JJA average 700 hPa isotachs from the NCEP-NCAR reanalysis.

576
577 Fig. 4 Frequency of occurrence of the core isertel value for each reanalysis time series in (a) the
578 STJ layer and (b) the POLJ layer. Solid blue, red and green lines in (a) and (b) are the SH
579 distributions from the NCEP, JRA55 and ERA5, respectively. The dashed blue, red and green
580 lines are the NH distributions from the NCEP, JRA55 and ERA5 reanalyses, respectively. In (b),
581 the NH distributions are from the 315:330K layer which houses the POLJ in the boreal winter.
582 Thin blue, red and green lines in (a) and (b) indicate the peak values of the core isertel in each
583 layer from each data set. Isertel values are given in potential vorticity units (PVU,
584 $1 \text{ PVU} = 10^6 \text{ K m}^2 \text{ kg}^{-1} \text{ s}^{-1}$), and are multiplied by -1 for the NH values.

585
586 Fig. 5 Seasonal average ALD (in degrees) of the SH wintertime subtropical and polar jets for
587 each cold season in the three reanalysis time series. The polar jet values are in the three shades
588 of blue while the subtropical jet values are in the three three shades of red. The dashed black line
589 through each time series represents the trend line for each (derived from the JRA-55 time series)
590 and is significant at the 96% level. Gray lines are the boreal winter ALD analysis from Fig. 6 of
591 Martin (2021). The “YEAR” on the abscissa indicates the year in which December of that cold
592 season occurred.

593
594 Fig. 6 Time series of the daily ALD of the polar (blue lines) and subtropical (red lines) jets from
595 the (a) NCEP-Reanalysis, (b) JRA-55, and (c) ERA5 data sets for austral winter 1999. The
596 correlation between the two times series from each data set is indicated.

Deleted: 4

Deleted: 5

Formatted: Header

599

600 Fig. 7 Seasonal average U along the core isertel for the subtropical (red lines) and polar (blue
601 lines) jets from each of the three SH reanalysis data sets. The thin black lines are trend lines for
602 each time series from the JRA-55 data. Gray lines are the equivalent boreal winter U analysis
603 from Fig. 9 of Martin (2021).

Deleted: 6

604

605 Fig. 8 Time series of the seasonal average equivalent latitude of the polar (blue lines) and
606 subtropical (red lines) jets from the three different SH reanalysis data sets. The thin black lines
607 are the trend lines (from the JRA-55 data) and are significant above the 99% leve for both jet
608 species. Gray lines are the boreal winter equivalent latitude analysis from Fig. 10 of Martin
609 (2021).

Deleted: 7

610

611 Fig. 9 JJA average SAM index (histogram) from NCEP's Climate Prediction Center. The index
612 is calculated by projecting the daily 700 hPa geopotential height anomalies poleward of 20S onto
613 the leading pattern of the Antarctic Oscillation (AAO) ofGong and Wang (1999). Black solid
614 line is theJJA average ALD of the POLJ from the JRA-55 reanalysis.

Deleted: 8

615

616 Fig. 10 Spaghetti plots of core isertels from SH summer months with maximum positive (red)
617 and negative (blue) SAM indices since 1979. (a) Daily JRA-55 core isertels from June 2009, the
618 June with the most positive SAM in the record. (b) As for Fig. 10a but for June 1992, the June
619 with the most negative SAM in the record. (c) As for Fig. 10a but for July 1998. (d) As for Fig.
620 10b but for July 1995. (e) As for Fig. 10a but for August 1994. (f) As for Fig. 10b but for
621 August 1981. Average ALD for the given months are listed in the bottom left of each panel.

Formatted: Header

625

626 [Fig. 11](#) 500 hPa height differences between the composite waviest and least wavy (a) polar jet
627 and (b) subtropical jet seasons constructed from the JRA-55 reanalysis. See Table 1 for
628 identification of the specific years comprising each composite. Positive (negative) height
629 differences are in solid red (blue) lines labeled in m and contoured every 10 m (-10 m) beginning
630 at 10 m (-10 m).

631

632 [Fig. 12](#) 250 hPa height differences between the composite waviest and least wavy (a) polar jet
633 and (b) subtropical jet seasons constructed from the JRA-55 reanalysis. See Table 1 for
634 identification of the specific years comprising each composite. Positive (negative) height
635 differences are in solid red (blue) lines labeled in m and contoured every 10 m (-10 m) beginning
636 at 10 m (-10 m).

637

638 [Fig. 13](#) 50 hPa height differences between the composite waviest and least wavy (a) polar jet
639 and (b) subtropical jet seasons constructed from the JRA-55 reanalysis. See Table 1 for
640 identification of the specific years comprising each composite. Positive (negative) height
641 differences are in solid red (blue) lines labeled in m and contoured every 10 m (-10 m) beginning
642 at 10 m (-10 m).

643

644

645

Deleted: 9

Deleted: 10

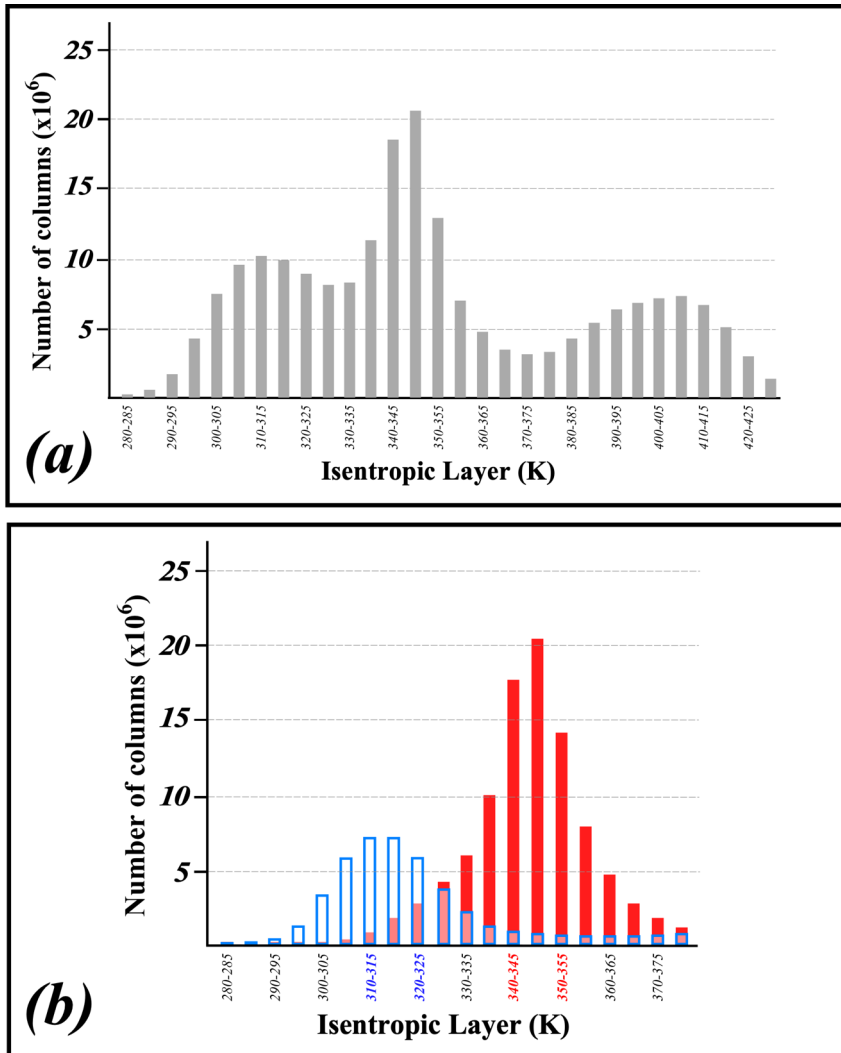


Fig. 1 (a) Distribution of grid-column maximum wind speeds found in 5K isentropic layers from 10 - 80°S for every 6h analysis time in JJA from 1958-2019 from the JRA-55 reanalysis. (b) As for Fig. 1a except limited to (i) grid-columns in which the integral average wind speed from 400 to 100 hPa exceeded 30 m s⁻¹ and (ii) to latitudes 0 - 40°S for the STJ and (iii) latitudes 40 to 65°S for the POLJ.

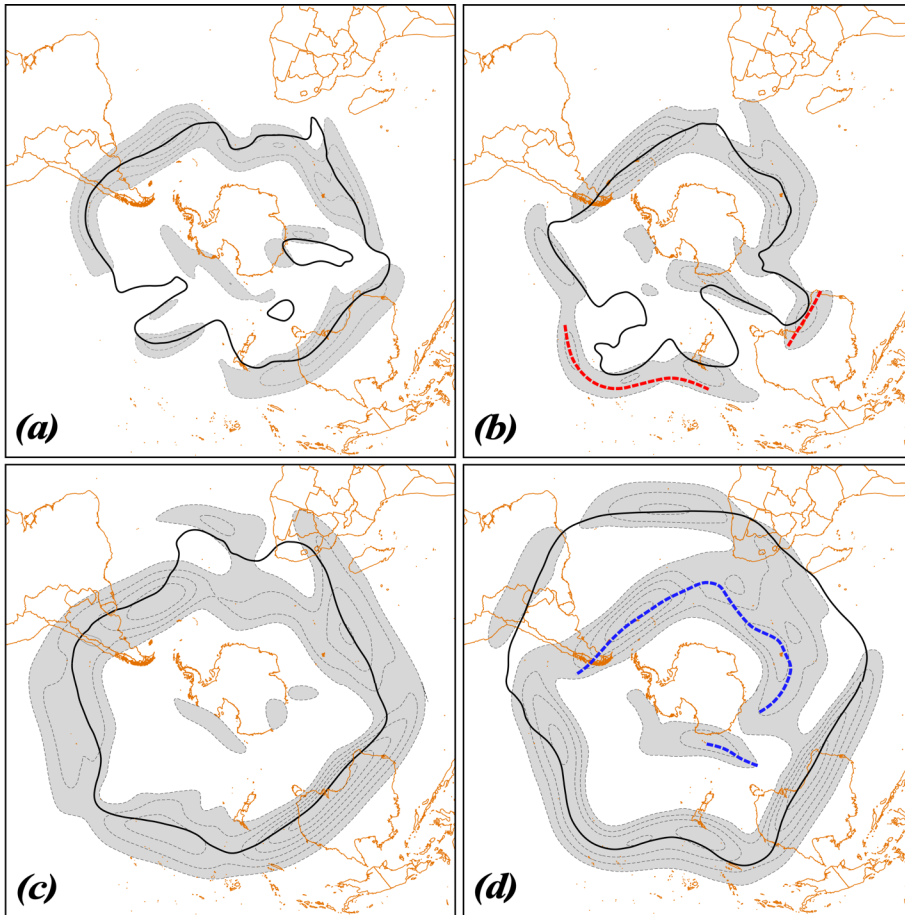


Fig. 2 (a) Isotachs of the daily averaged wind speed (contoured every 10 m s^{-1} and shaded above 30 m s^{-1}) and the core isertel (bold black line) in the 310:325K isentropic layer on 13 July 1995 from the JRA-55 reanalysis data. The core isertel value is -1.3 PVU. (b) As in (a) but for 24 August 2001. Core isertel value is -2.0 PVU. Dashed red line indicates portion of the core isertel from the overlying STJ layer (depicted in Fig. 2d). (c) As in (a) but for wind speeds and core isertel in the 340:355K isentropic layer on 13 July 1995. Core isertel value is -3.6 PVU. (d) As in (c) but for 24 August 2001. Core isertel value is -1.4 PVU. Dashed blue line indicates a portion of the core isertel from the underlying POLJ layer (depicted in Fig. 2b). See text for further explanation.

649

650

651

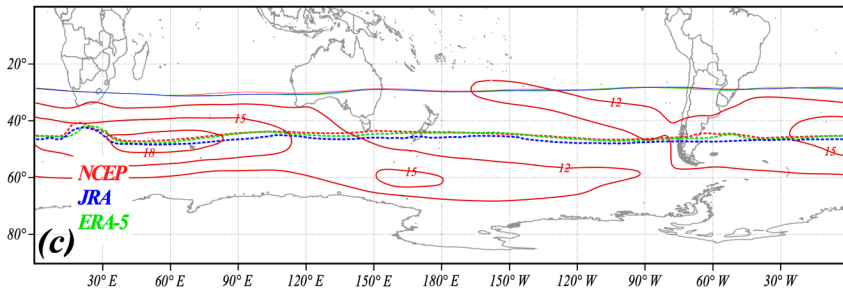
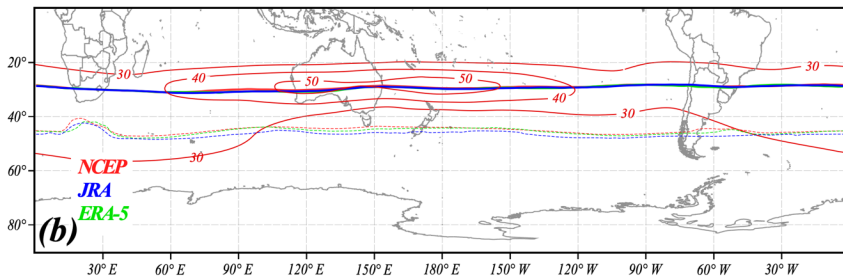
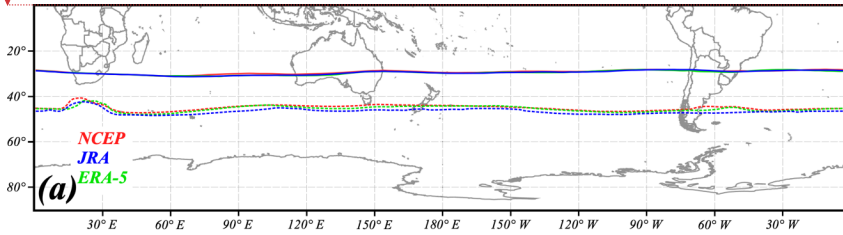


Fig. 3 (a) Solid (dashed) lines are the positions of the average core isertels of the STJ (POLJ) from each of the three reanalyses employed in this study. The different reanalyses are color coded. (b) Thick solid lines are the positions of the average core isertels for the STJ from each of the reanalyses superimposed with JJA average 200 hPa isotachs from the NCEP-NCAR reanalysis. (c) Thick dashed lines are the positions of the average core isertels for the POLJ superimposed with JJA average 700 hPa isotachs from the NCEP-NCAR reanalysis.

652

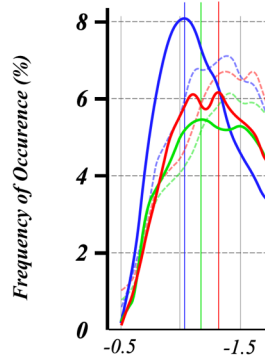
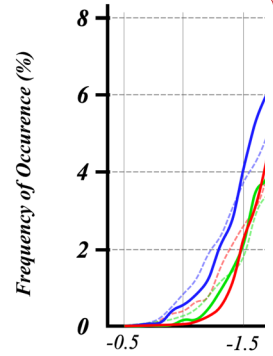


Fig. 3 Frequency of occurrence of the core isertels of the STJ (POLJ) from each of the three reanalyses employed in this study. The different reanalyses are color coded. (b) Thick solid lines are the positions of the average core isertels for the STJ from each of the reanalyses superimposed with JJA average 200 hPa isotachs from the NCEP-NCAR reanalysis. (c) Thick dashed lines are the positions of the average core isertels for the POLJ superimposed with JJA average 700 hPa isotachs from the NCEP-NCAR reanalysis.

Deleted: 1 PVU = $10^6 \text{ K m}^2 \text{ kg}^{-1} \text{ s}^{-1}$) and are multiple
Page Break

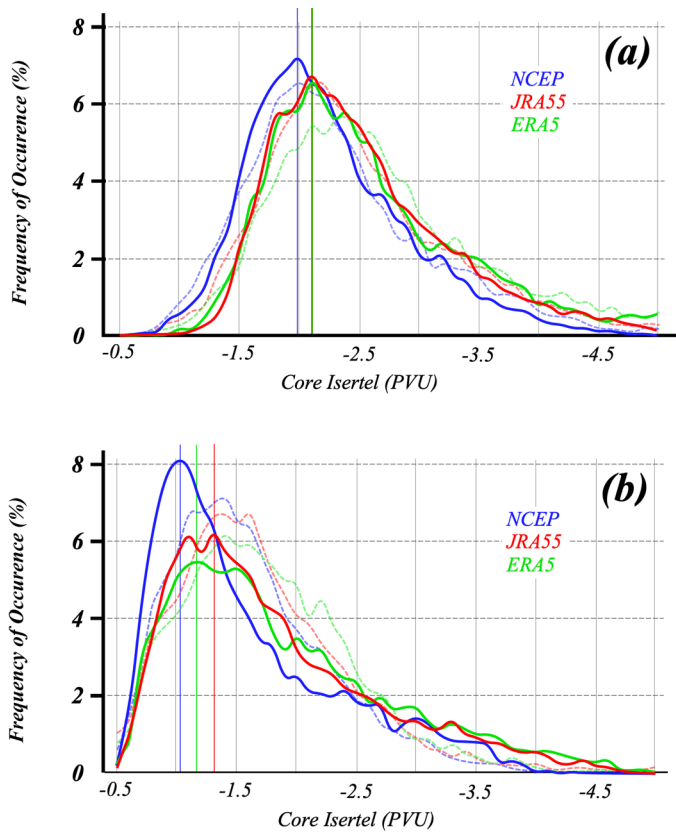


Fig. 4 Frequency of occurrence of the core isertel value for each reanalysis time series in (a) the STJ layer and (b) the POLJ layer. Solid blue, red and green lines in (a) and (b) are the SH distributions from the NCEP, JRA55 and ERA5, respectively. The dashed blue, red and green lines are the NH distributions from the NCEP, JRA55 and ERA5 reanalyses, respectively. In (b), the NH distributions are from the 315:330K layer which houses the POLJ in the boreal winter. Thin blue, red and green lines in (a) and (b) indicate the peak values of the core isertel in each layer from each data set. Isertel values are given in potential vorticity units (PVU, $1 \text{ PVU} = 10^6 \text{ K m}^2 \text{ kg}^{-1} \text{ s}^{-1}$) and are multiplied by -1 for the NH values.

656

657

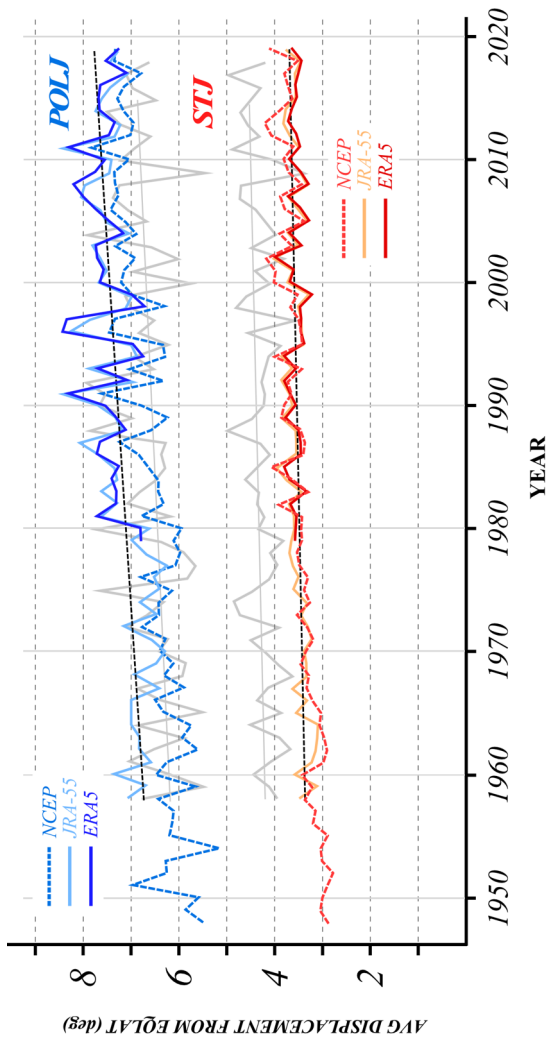


Fig. 5 Seasonal average ALD (in degrees) of the SH wintertime subtropical and polar jets for each cold season in the three reanalysis time series. The polar jet values are in the three shades of blue while the subtropical jet values are in the three shades of red. The dashed black line through each time series represents the trend line for each (derived from the JRA-55 time series) and is significant at the 96% level. Gray line is the boreal winter average ALD from 1958 onward portrayed in Fig. 6 of Martin (2021). The “YEAR” on the abscissa indicates the year in which December of that cold season occurred.

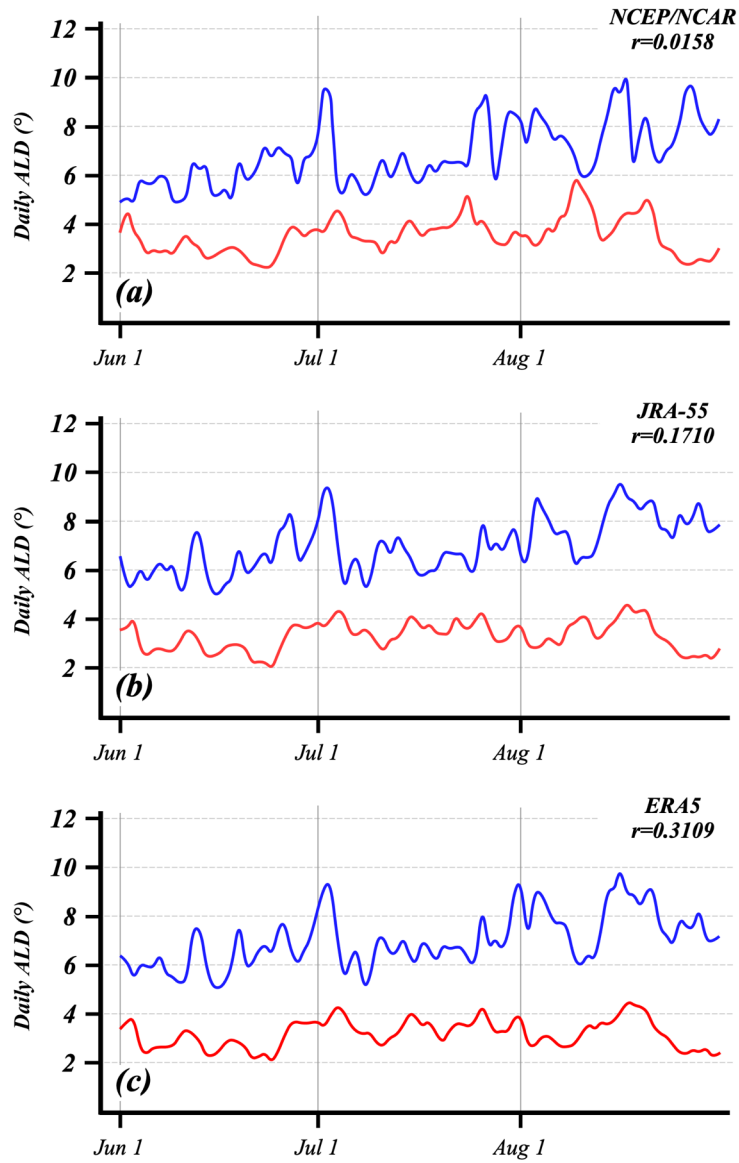


Fig. 6 Time series of the daily ALD of the polar (blue lines) and subtropical (red lines) jets from the (a) NCEP-Reanalysis, (b) JRA-55, and (c) ERA5 data sets for austral winter 1999. The correlation between the two times series from each data set is indicated.

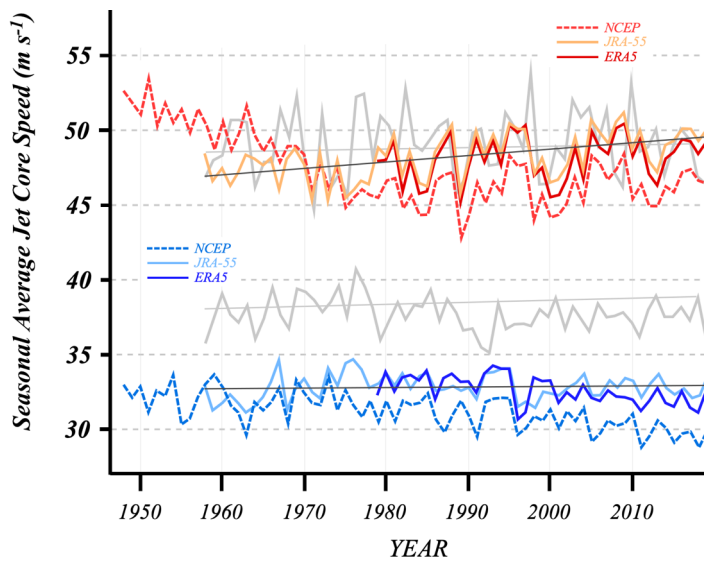


Fig. 7 Seasonal average U along the core isertel for the subtropical (red lines) and polar (blue lines) jets from each of the three SH reanalysis data sets. The thin black lines are trend lines for each time series from the JRA-55 data. Gray line is the average (1958-2018) boreal winter U analysis for each jet from the three data sets in Fig. 9 of Martin (2021).

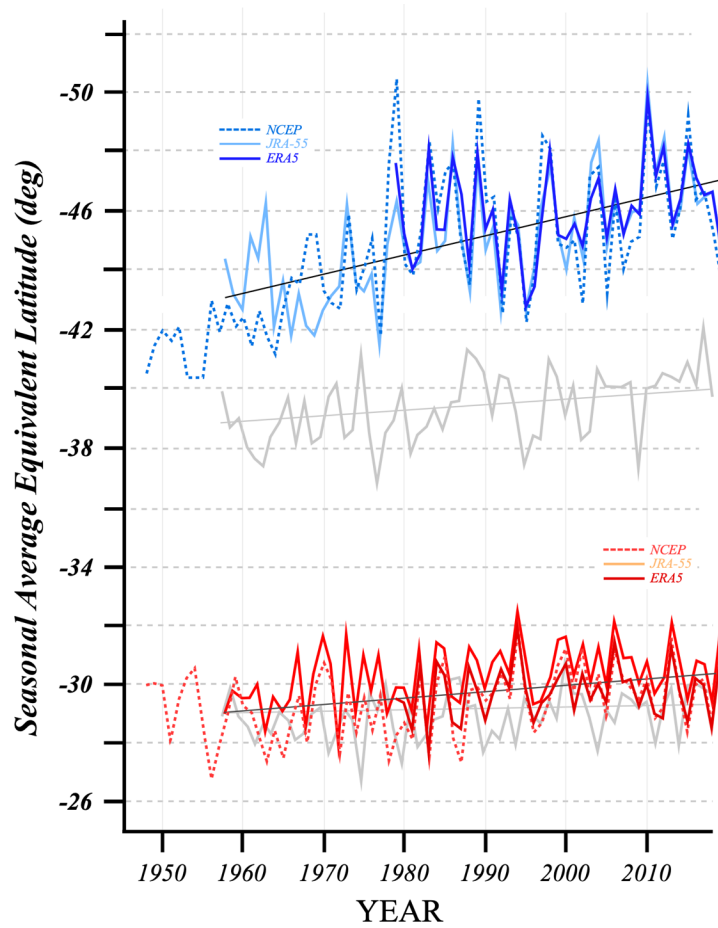


Fig. 8 Time series of the seasonal average equivalent latitude of the polar (blue lines) and subtropical (red lines) jets from the three different SH reanalysis data sets. The thin black lines are the trend lines (from the JRA-55 data) and are significant above the 99% level for both jet species. Gray line is the boreal winter average (1958-2017) equivalent latitude for each jet from the three reanalysis data sets portrayed in Fig. 10 of Martin (2021).

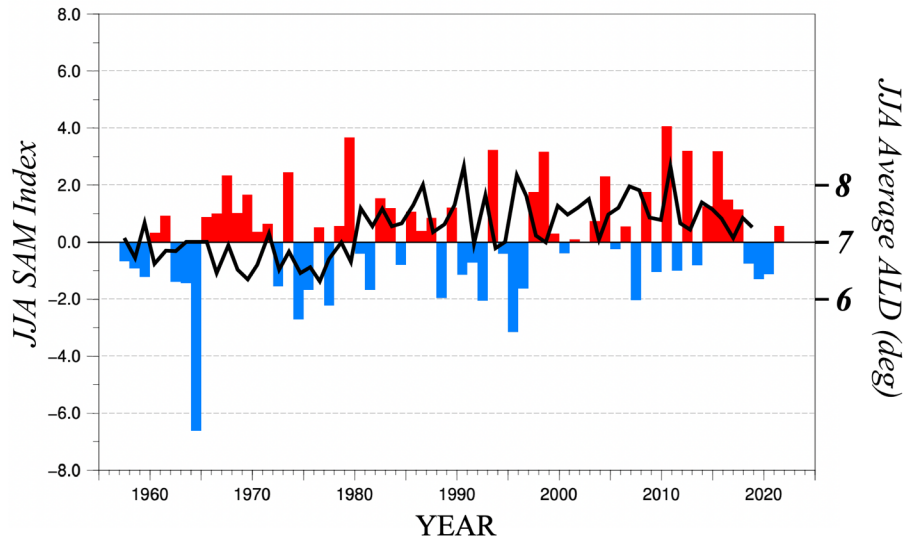


Fig. 9 JJA average SAM index (histogram) from NCEP's Climate Prediction Center. The index is calculated by projecting the daily 700 hPa geopotential height anomalies poleward of 20S onto the leading pattern of the Antarctic Oscillation (AAO) of Gong and Wang (1999). Black solid line is the JJA average ALD of the POLJ from the JRA-55 reanalysis.

668
669

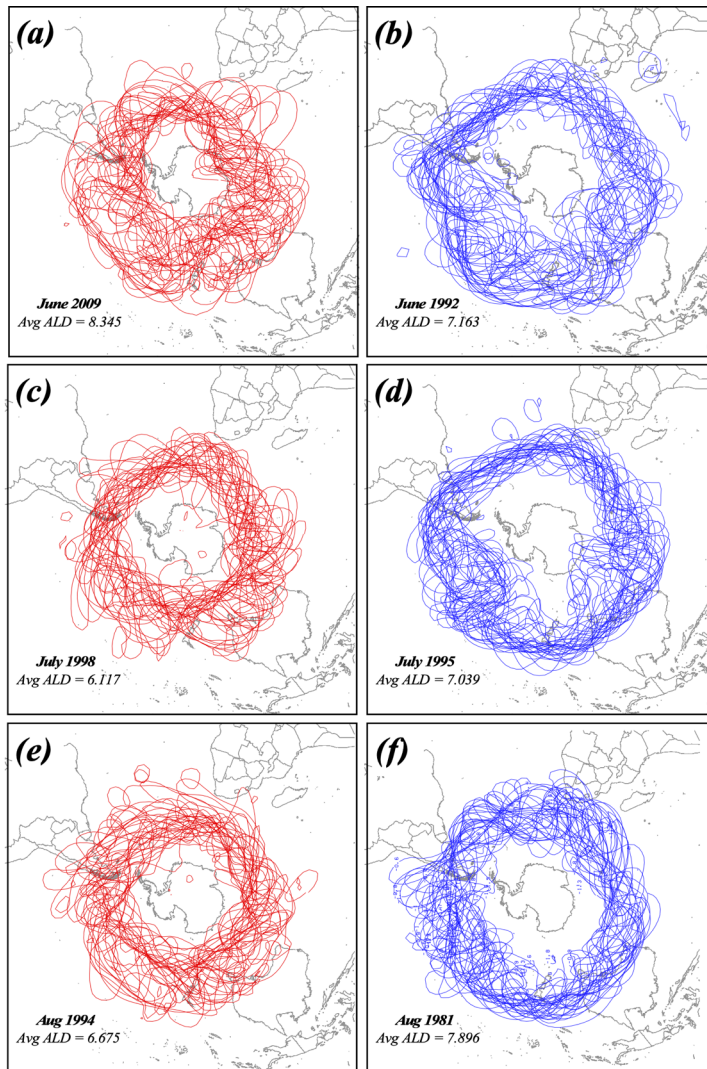


Fig. 10 Spaghetti plots of core isertels from SH summer months with maximum positive (red) and negative (blue) SAM indices since 1979. (a) Daily JRA-55 core isertels from June 2009, the June with the most positive SAM in the record. (b) As for Fig. 10a but for June 1992, the June with the most negative SAM in the record. (c) As for Fig. 10a but for July 1998. (d) As for Fig. 10b but for July 1995. (e) As for Fig. 10a but for August 1994. (f) As for Fig. 10b but for August 1981. Average ALD for the given months are listed in the bottom left of each panel.

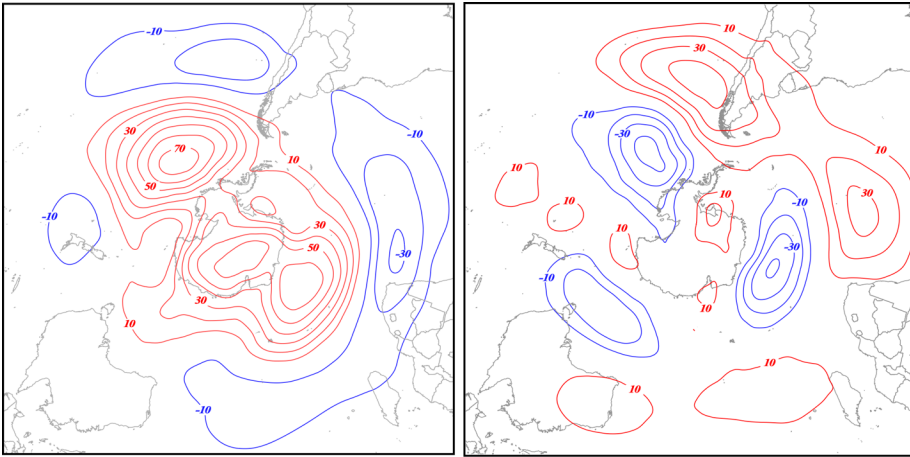


Fig. 11 500 hPa height differences between the composite waviest and least wavy (a) polar jet and (b) subtropical jet seasons constructed from the JRA-55 reanalysis. See Table 1 for identification of the specific years comprising each composite. Positive (negative) height differences are in solid red (blue) lines labeled in m and contoured every 10 m (-10 m) beginning at 10 m (-10 m).

671

672

673

674

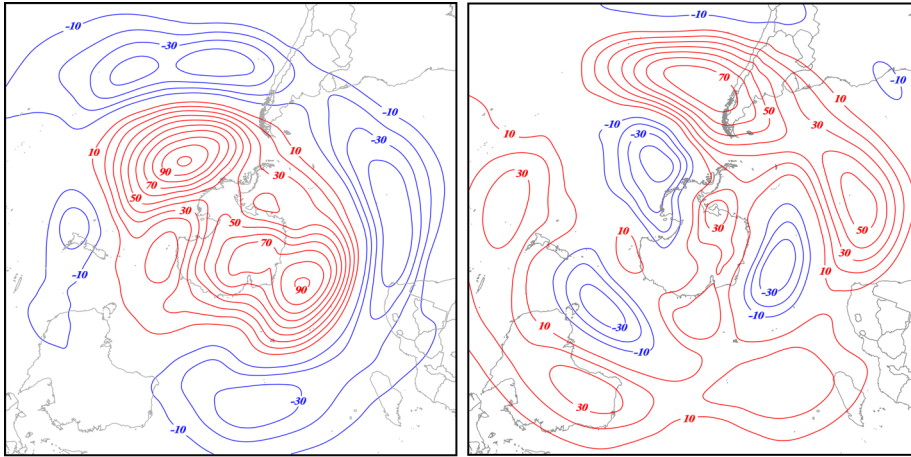


Fig. 12 250 hPa height differences between the composite waviest and least wavy (a) polar jet and (b) subtropical jet seasons constructed from the JRA-55 reanalysis. See Table 1 for identification of the specific years comprising each composite. Positive (negative) height differences are in solid red (blue) lines labeled in m and contoured every 10 m (-10 m) beginning at 10 m (-10 m).

675

676

677

678

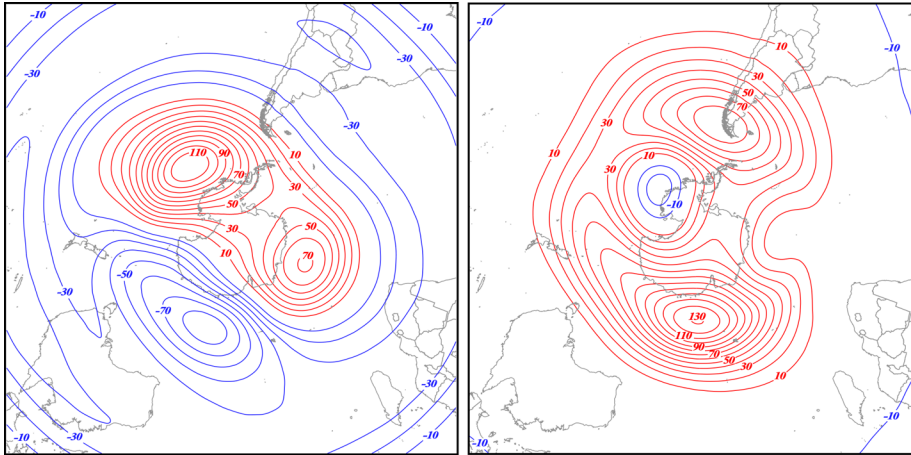


Fig. 13 50 hPa height differences between the composite waviest and least wavy (a) polar jet and (b) subtropical jet seasons constructed from the JRA-55 reanalysis. See Table 1 for identification of the specific years comprising each composite. Positive (negative) height differences are in solid red (blue) lines labeled in m and contoured every 10 m (-10 m) beginning at 10 m (-10 m).

